Journal of Materials Science & Technology 187 (2024) 72–85

Contents lists available at ScienceDirect

Journal of Materials Science & Technology

journal homepage: www.elsevier.com/locate/jmst

Research Article

TiZrHfNb refractory high-entropy alloys with twinning-induced plasticity

Shubin Wang[a], Da Shu[a,*], Peiying Shi[b], Xianbing Zhang[c], Bo Mao[a], Donghong Wang[a], Peter. K. Liaw[d,*], Baode Sun[a,*]

[a] Shanghai Key Lab of Advanced High-temperature Materials and Precision Forming and State Key Lab of Metal Matrix Composites, School of Materials Science and Engineering, Shanghai Jiao Tong University, Shanghai 200240, China
[b] Shanghai Institute of Applied Physics, Chinese Academy of Sciences, Shanghai 201800, China
[c] Department of Mechanical and Energy Engineering, Southern University of Science and Technology, Shenzhen 518055, China
[d] Department of Materials Science and Engineering, The University of Tennessee, Knoxville, TN, 37996, USA

ARTICLE INFO

Article history:
Received 15 August 2023
Revised 12 November 2023
Accepted 20 November 2023
Available online 10 January 2024

Keywords:
Refractory high-entropy alloys
Cryogenic temperature
Twinning induced plasticity
Hierarchical twins
Tensile properties

ABSTRACT

The twinning-induced plasticity (TWIP) effect has been widely utilized in austenite steels, β-Ti alloys, and recently developed face-centered-cubic (FCC) high-entropy alloys (HEAs) to simultaneously enhance the tensile strength and ductility. In this study, for the first time, the TWIP effect through hierarchical {332<113> mechanical twinning has been successfully engineered into the TiZrHfNb refractory HEAs by decreasing temperature and tailoring the content of Nb to destabilize the BCC phase. At cryogenic temperature, the comprehensive hierarchical {332}<113> mechanical twins are activated in $TiZrHfNb_{0.5}$ alloy from micro- to nanoscale and progressively segment the BCC grains into nano-scale islands during deformation, ensuring sustainable strain hardening capability and eventually achieving a substantial 35 % uniform tensile elongation. In addition, at 77 K, the tensile strength and uniform elongation of $TiZrHfNb_x$ alloys can further be adjusted by a moderate increase of Nb. The results above shed new light on the development of high-performance refractory HEAs with a high and adjustable strength and ductility combination down to the cryogenic temperature.

1. Introduction

In the past decade, refractory high-entropy alloys (RHEAs) which usually contain at least 4 of the 9 refractory elements (Cr, Hf, Mo, Nb, Ta, Ti, V, W, and Zr) have attracted extensive research interest due to their promising properties under extreme conditions [1–4]. As a prototype RHEA, an equiatomic TiZrHfNbTa proposed by Senkov [5] exhibits high strength and ductility combination [6–8]. However, rooted in the dominant deformation mechanism of screw dislocation glide [6,8], it remains challenging to keep substantial uniform ductility which relies on sufficient strain hardening ability under uniaxial tensile deformation [9,10]. By promoting mechanical twinning in competition with the motion of dislocations, the twinning-induced plasticity (TWIP) effect can be activated to govern the plastic deformation of solid solution alloys [11–14]. This TWIP effect fundamentally results from the huge strain hardening capability which delays the onset of plastic instability (necking) [15–18]. Therefore, in this study, the TWIP effect is explored to endow RHEAs with strong strain-hardening behavior and thereby the high strength-ductility combination.

The TWIP effect has been widely adopted in advanced Fe-Mn-based austenitic steels [11,12,17,19,20], metastable β titanium alloys [13,18,21–23], and face-centered-cubic (FCC) 3d-transition HEAs [15,24–28] with low stacking fault energy. Compared with the extensively investigated FCC HEAs, the TWIP effect is rarely observed in the BCC-structured RHEAs [9,29]. Based on the design strategy of "metastable engineering", the transformation-induced plasticity (TRIP) effect has been utilized to improve the strain-hardening rate of refractory HEAs with the compositions of $Ti_{35}Zr_{27.5}Hf_{27.5}Nb_5Ta_5$ [30], $TiZrHfTa_x$ (x = 0.4, 0.5, and 0.6) [31] and $Ti_{55-x}Zr_{20}Hf_{15}Al_{10}Nb_x$ (x = 4–8) [32]. Different from $Ti_{35}Zr_{27.5}Hf_{27.5}Nb_5Ta_5$ and $Ti_{55-x}Zr_{20}Hf_{15}Al_{10}Nb_x$ alloys above which activate the orthorhombic α'' phase during deformation, the improvement of tensile ductility of the metastable $TiZrHfTa_x$ alloys resorts to the hexagonal α phase. However, the deformation-induced $\beta \rightarrow \alpha'$ and $\beta \rightarrow \alpha''$ transformation revealed in the metastable $TiZrHfNb_x$ (x = 0.2, 0.4) alloys strongly deterio-

* Corresponding authors.
E-mail addresses: dshu@sjtu.edu.cn (D. Shu), pliaw@utk.edu (P.K. Liaw), bdsun@sjtu.edu.cn (B. Sun).

https://doi.org/10.1016/j.jmst.2023.11.047
1005-0302/

rate the compression plasticity compared to the stable $TiZrHfNb_x$ (x = 0.6, 1) alloys rather than improving it [33]. The TWIP effect is usually accompanied by the TRIP effect in both FCC HEAs [24,25] and metastable β-Ti alloys [21,34]. A moderate increase of the stacking fault energy in FCC HEAs [24–26] or appropriately increasing the stability of the BCC phase of metastable β-Ti [22] can promote the mechanism transition from TRIP to TWIP. However, twinning-induced plasticity has not yet been discovered for metastable refractory HEAs, which indicates that the compositional space that can trigger this effect may be quite narrow.

Apart from the alloy composition, the temperature is another crucial factor to affects the competitive-deformation mechanisms between the dislocation slip and mechanical twinning [15,35–38]. Extensive twinning is expected to occur at low temperatures when the critical stress for dislocation slips sharply increases while the twinning stress remains almost constant with decreasing temperature [38]. With reducing the temperature, the predominated deformation mechanisms of CrMnFeCoNi [15,36] and CrCoNi [35,37] alloys transform from the dislocation slip at 293 K to mechanical twinning at 77 K. Attributing to the strong strain-hardening behavior caused by mechanical twinning, the uniform ductility and fracture toughness of FCC HEAs are significantly improved at cryogenic temperature [15,35,39]. The {111}<112> mechanical twinning makes the CrCoNi alloy a strong competitor to the best cryogenic alloy even at the liquid-helium temperature [39]. The yield strength of BCC metals and alloys is strongly dependent on the deformation temperature [38], which could provide sufficient critical shear stress to trigger mechanical twinning [38]. For the equiatomic TiZrHfNbTa alloy [7], the {112}<111> mechanical twinning can be activated at cryogenic temperatures, which contributes to moderate tensile ductility. However, the strain-hardening rate is still negligible due to the lack of sufficient twin fractions and twin-twin intersections.

To explore refractory high-entropy alloys with twinning-induced plasticity (TWIP-RHEAs), in this investigation, we destabilize the BCC structure of a prototype TiZrHfNb high-entropy alloy by decreasing the Nb content combined with decreasing deformation temperature to activation of {332}<113> mechanical twinning. Both the alloy composition and deformation temperature are controlled to provide a comprehensive understanding of the TWIP effect in metastable $TiZrHfNb_x$ HEAs.

2. Experimental methods

2.1. Alloys preparation

Three ingots weighed 500 g of non-equiatomic $TiZrHfNb_x$ (x = 0.5, 0.55, 0.6) alloys were prepared by levitation melting in a cold crucible under argon atmosphere. The purity of the raw materials of Ti, Zr, Hf, and Nb blocks was above 99.9 wt.%. The ingots were melted at least four times to achieve a homogeneous distribution of alloy elements. After the last melting process, the alloy melts were finally dropped to the bottom of the crucible and solidified into ingots. The ingots were annealed at 1300 °C for 10 h in a circulating argon atmosphere to homogenize the microsegregation, followed by water quenching. The cold rolling with a total thickness reduction of about 80 % (from 10 to 2 mm) combined with recrystallization treatments at 1000 °C for 30 min was used to acquire microstructures with equiaxed grains. Table S1 in Supplementary Materials gives the chemical compositions of these $TiZrHfNb_x$ alloys and also O/N/H impurities content.

2.2. Tensile tests and microstructure characterization

The tensile specimens with a gauge length of 16 mm and a cross-section area of 4 mm × 1.8 mm were sectioned from the plates along the rolling direction (RD). The tensile specimens were ground step by step using SiC sandpapers from #80, #120, #240, #400, and #800 to remove the surface oxidation and other defects. The uniaxial tensile tests were conducted employing an MTS-SANS CMT5000 mechanical testing system equipped with a dewar tank to ensure the test temperature was continuously adjustable from 77 K to room temperature. Before each test, the specimen was immersed at the set temperature for at least 10 min to maintain a uniform temperature distribution of the sample. The crystallographic structures of the samples were identified on a D8 ADVANCE Da Vinci X-ray diffraction (XRD) device with Cu-$K_{\alpha 1}$ radiation (λ = 0.154 nm) at a 2θ range of 20°–100° at a scanning speed of 2° min^{-1} and with a step size of 0.02° The samples for XRD tests were ground with sandpaper (2000 mesh). The alloy composition was measured by the EDS quantitative area scanning using a Mira3 Field Emission scanning electron microscope (SEM). The deformation substructures were characterized by backscattered electron (BSE) and electron backscattered diffraction (EBSD) detectors using an SEM and transmission electron microscope (TEM, FEI Talos F200X G2). Samples for SEM-BSE and EBSD were mechanically and electrochemically polished with 10 vol.% $HClO_4$ in a CH_4O solution at −35 °C. Samples for TEM were prepared by using twin-jet electro-polishing, followed by ion-beam milling.

3. Results

3.1. Temperature-dependent tensile properties and microstructure of $TiZrHfNb_{0.5}$ alloy

The tensile properties of the $TiZrHfNb_{0.5}$ alloy and related microstructure evolution are shown in Fig. 1. Fig. 1(a) presents the engineering tensile stress-strain curves of $TiZrHfNb_{0.5}$ alloy at room temperature (RT, ~ 300 K), 127 K, and 77 K, respectively. At RT, the uniform elongation is less than 5 % although the total tensile elongation reaches 20 %, indicating poor strain-hardening and a long period of necking stage soon after yielding. At 127 K, the sustaining strain-hardening ability enables nearly 30 % uniform tensile strain. With the deformation temperature continuing down to 77 K, the uniform tensile strain increases to 35 %. With decreasing temperature, the tensile strength, especially the engineering tensile strength is significantly improved. According to X-ray diffraction (XRD) results, in Fig. 1(b), the $TiZrHfNb_{0.5}$ alloy always maintains a single-phase BCC structure after tensile deformation at three temperatures.

As exhibited in Fig. 1(c), the initial microstructure of single-phase BCC equiaxed grains with coarse grains was obtained through homogenization, cold rolling, and recrystallization processes. At the nanoscale, Fig. S1(a1–a3) shows a small number of athermal ω nanoparticles dispersed in the BCC matrix of the as-recrystallized $TiZrHfNb_{0.5}$ alloy. Fig. 1(d1–d3) shows the fracture morphologies of the samples at RT, 127 K, and 77 K, respectively. For these samples, micron-sized dimples dominate the fracture processes and are consistent with the significant necking behavior in these stress-strain curves, which confirms the intrinsic ductility of $TiZrHfNb_{0.5}$ alloy at cryogenic temperatures. Fig. 1(e) shows the deformation substructures evolution of the $TiZrHfNb_{0.5}$ alloy interrupted at different tensile strains at 77 K. These straight deformation bands are distributed in almost all grains with variant orientations in the entire field of view. With increasing the tensile strain from 5 % to 35 %, the continuously activated deformation bands progressively divide the matrix into micron-scale fine domains. In Fig. S2(a1–c1), when deformation at RT, a small number of thick kink bands [40] with arbitrary misorientation range from 15° to 20° rather than high-density straight bands distributed inside the deformed grains. As shown in Fig. S2(d1), the deformation

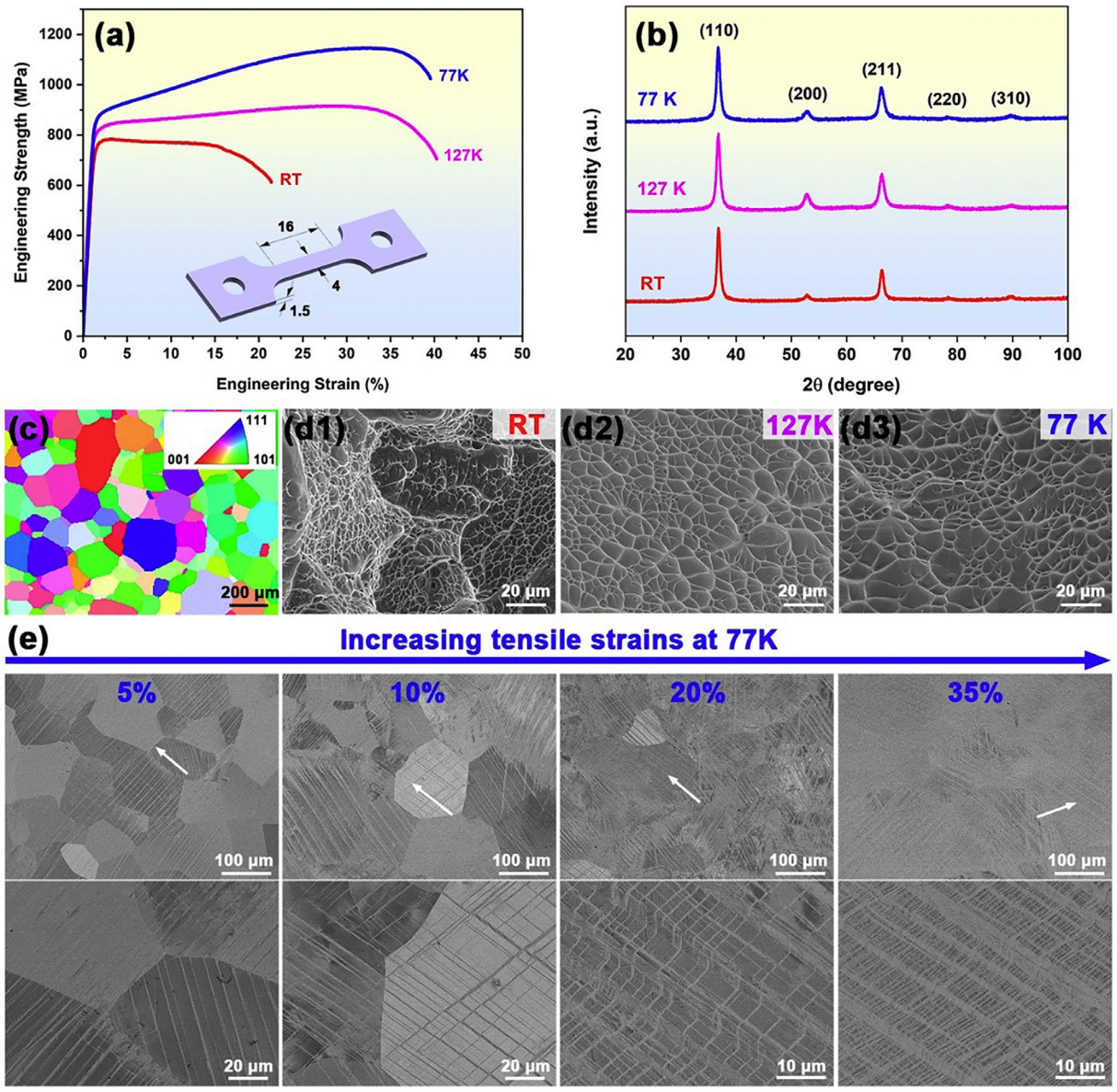

Fig. 1. Microstructures and tensile properties of the $TiZrHfNb_{0.5}$ alloy: (a) engineering tensile stress-strain curves with an inset of the tensile sample and (b) X-ray diffraction (XRD) patterns at room temperature (RT), 127 K, and 77 K, respectively; (c) initial as-recrystallized microstructure; (d1–d3) fracture morphologies at RT, 127 K, and 77 K, respectively; (e) deformation substructures under (BSE) image with increasing the tensile strain from 5 % to 35 % at 77 K.

mechanism of the $TiZrHfNb_{0.5}$ alloy is completely controlled only by dislocation slip at RT.

3.2. Deformation-driven hierarchical twinning in the $TiZrHfNb_{0.5}$ alloy

The wide-field deformation microstructure of $TiZrHfNb_{0.5}$ alloy at 77 K is presented in Fig. 2. Using electron backscattered diffraction (EBSD), these deformation bands above are characterized to be {332}<113> mechanical twins. The {332}<113> deformation twins are activated in almost all of the recrystallized grains, and their density improved with increasing the tensile strain from 10 to 20 %.

In Fig. 3(a, b), two variants of {332}<113> twins with a width of several micrometers intersect with each other and divide the BCC matrix into regular block regions. In Fig. 3(c), the crystallographic misorientations cross these two variants, and the matrix (red line in Fig. 3(b)) plotted is exactly consistent with the rotation angle of {332}<113> twins (50.5° rotation about the ⟨011⟩ axis corresponding to the coincidence site lattice, Σ11 interfaces), which commonly activated in metastable β titanium alloys [22,34,41]. To further illustrate the crystallographic orientations between the BCC matrix and two different twin variants, in Fig. 3(d–f), stereographic projection pole figures are constructed based on crystallographic orientation information. The $(32\bar{3})$ pole and $[\bar{1}31]$ direction of the BCC matrix coincides with the $(\bar{2}\bar{3}3)$ pole and $[3\bar{1}1]$ direction of the twin variant 1. Meanwhile, the $(\bar{3}23)$ pole and $[13\bar{1}]$ direction of the BCC matrix coincides with the $(\bar{3}\bar{2}3)$ pole and $[\bar{1}31]$ direction of the twin variant 2. The corresponding relations above confirm the $(32\bar{3})[\bar{1}31]$ and $(\bar{3}23)[13\bar{1}]$ deformation twinning variants of these bands. In addition, coincidentally, these two intersected variants share a common rotation axis of [101] of the BCC matrix during twinning.

In Fig. 4, using the EBSD characterization and pole-figures analysis, the evolved hierarchical {332}<113> twinning structures consisting of multiple and high-order twin variants span the scale from the micrometer to nanometer are activated in the $TiZrHfNb_{0.5}$

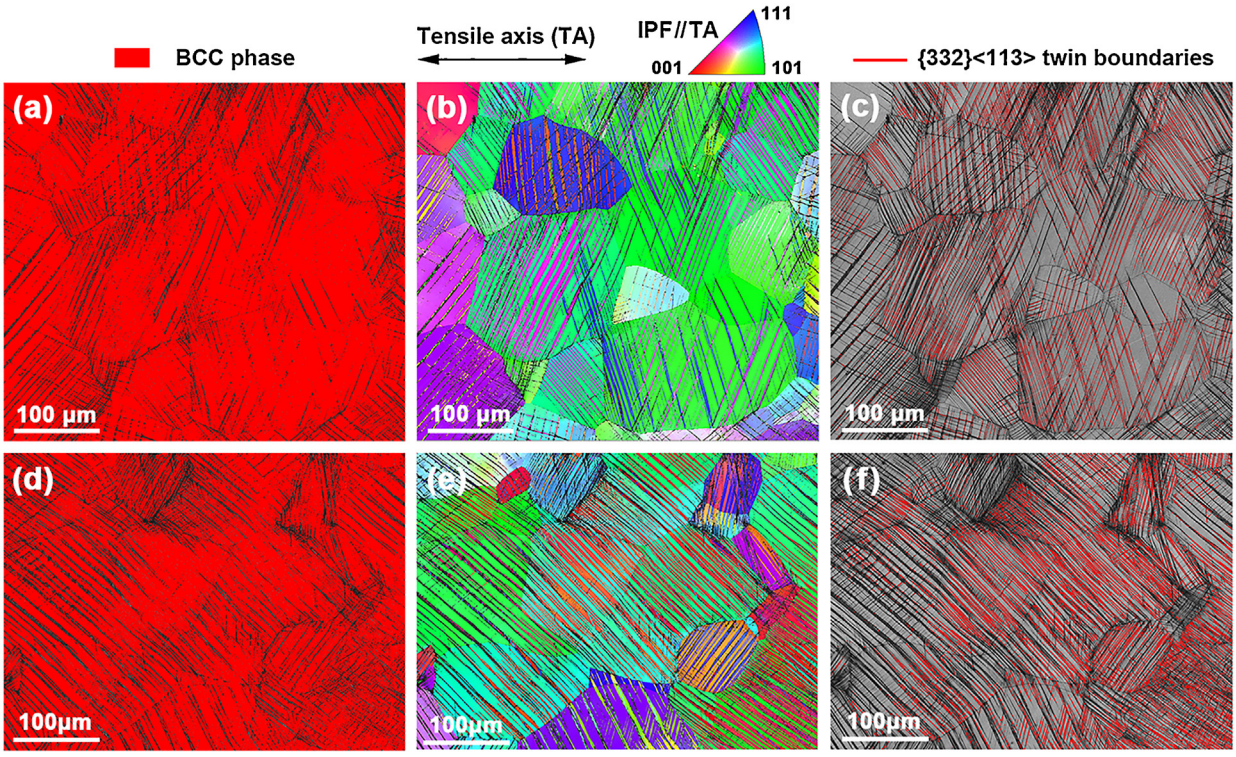

Fig. 2. Deformation microstructure of the $TiZrHfNb_{0.5}$ alloy after (a–c) 10 % and (d–f) 20 % tensile strain at 77 K: (a, d) phase diagrams; (b, e) inverse pole figures (IPFs) and (c, f) band contrast map overlapped with {332}<113> twin boundaries.

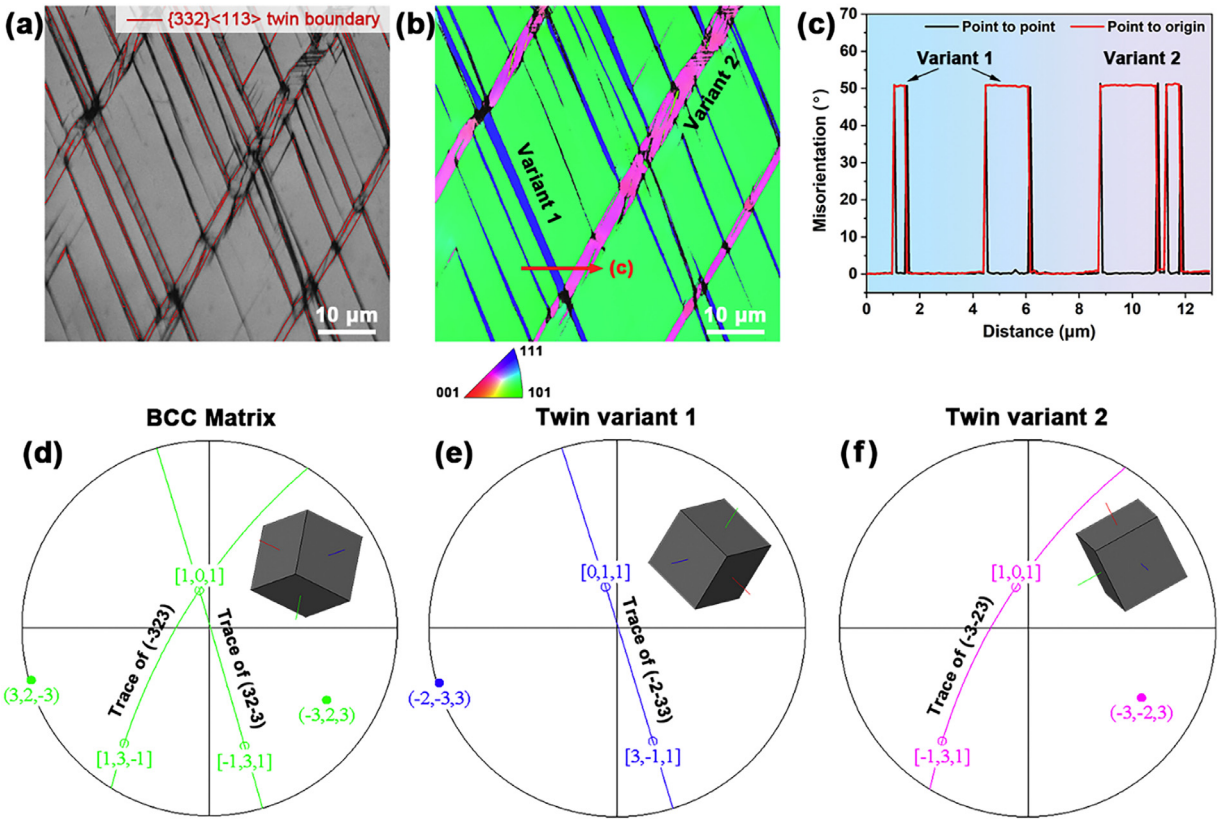

Fig. 3. {332}<113> mechanical twins in the $TiZrHfNb_{0.5}$ alloy after a 10 % tensile strain at 77K: (a) band contrast map overlapped with {332}<113> twin boundaries; (b) inverse pole figure (IPF) shows two twinning variants; (c) misorientation profiles of two twin variants along the red line in Fig. 2(b); (d–f) stereographic projection pole figures of the BCC matrix (green matrix), twin variant 1 (blue bands), and twin variant 2 (purple bands).

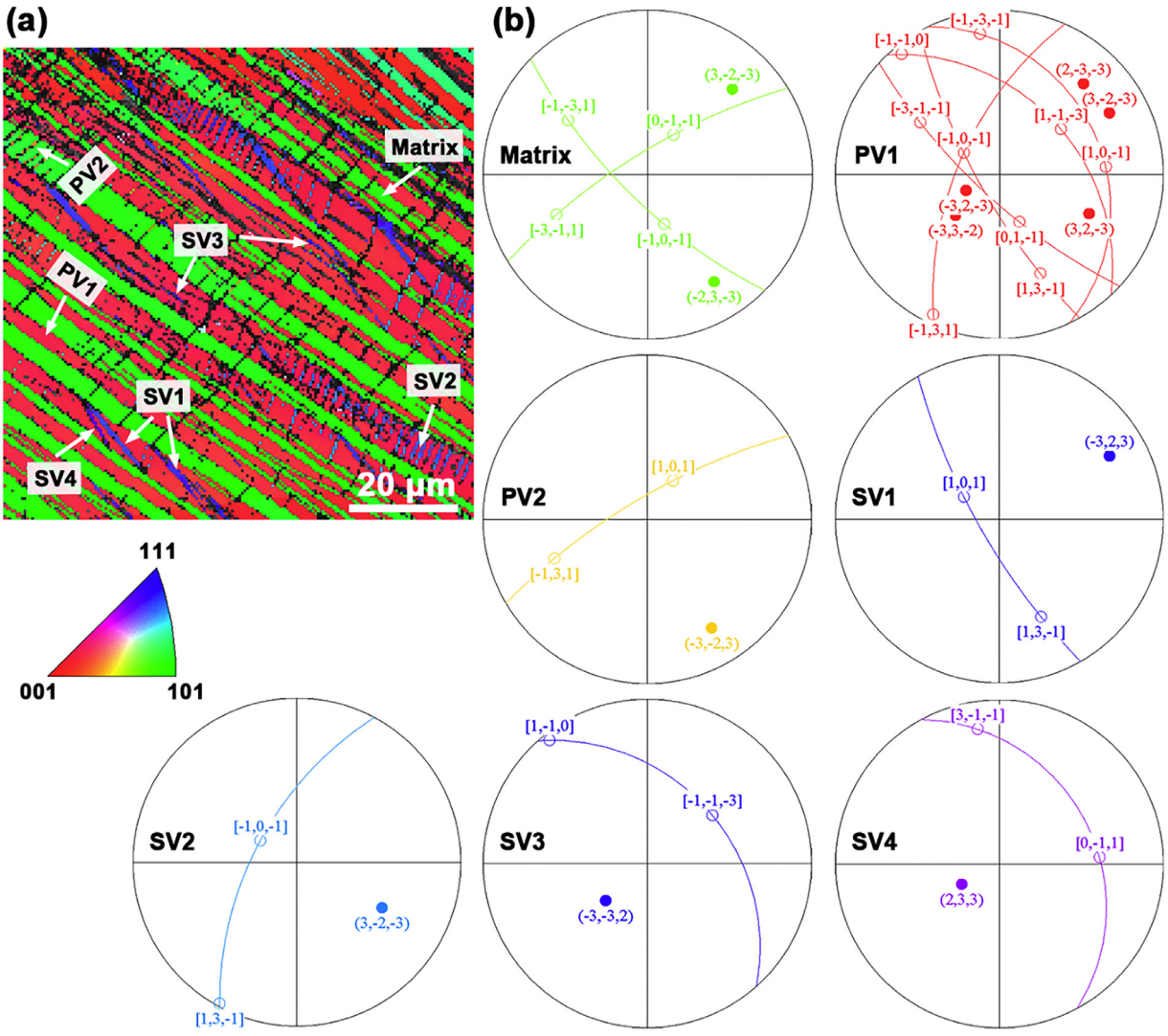

Fig. 4. Hierarchical {332}<113> mechanical twins of the $TiZrHfNb_{0.5}$ alloy at 77 K after 20 % tensile strain: (a) IPF; (b) stereographic projection of the BCC matrix and primary twins variants (PV1, PV2) and secondary twins variants (SV1, SV2, SV3, and SV4).

alloy during tensile at 77 K. Fig. 4(a) shows the zoom-in images of a grain Fig. 2(e). The matrix (with green color) is divided by primary twins variant 1 (PV1) $(3\bar{2}\bar{3})[\bar{1}\bar{3}1]$ and primary twins variant 2 (PV2) $(\bar{2}3\bar{3})[\bar{3}\bar{1}1]$ although the PV1 is dominant. Within the coarse PV1 bands, four secondary twin variants (SV1 $(3\bar{2}\bar{3})[13\bar{1}]$, SV2 $(32\bar{3})[\bar{1}31]$, SV3 $(\bar{3}3\bar{2})[1\bar{1}\bar{3}]$, and SV4 $(\bar{3}2\bar{3})[\bar{1}\bar{3}\bar{1}]$) are triggered to further refine the coarse PV1 bands themself.

In Fig. 5, transmission electron microscope (TEM) is used to further reveal the fine substructures of {332}<113> deformation twins at the nanoscale. Fig. 5(a) gives a bright-field (BF) image of a $(2\bar{3}\bar{3})[311]$ twinning band with a $[0\bar{1}1]$-axis selected area diffraction (SAED) pattern in Fig. 5(b). A high density of straight dislocation lines is arranged within the twin and on the twin interface on the (211) lattice plane in Fig. 5(a). Such a dislocation decorated {332}<113> mechanical twins structure has been reported previously in metastable β titanium alloys [22,34,42,43]. These dislocations were considered to be related to the intrinsic formation mechanisms of {332}<113> twinning, such as the atomic shuffling process [42], the detwinning-induced reverse motion of twin interface during unloading [43], or the detwinning and stress-relaxation accompanied by the reverse α'' martensitic transformation [22,34]. These high-density dislocations would render the twinned area harder than the BCC matrix and further impede the dislocation slip [22]. Fig. 5(c) shows a hierarchical {332}<113> twinning morphology with its corresponding SAED patterns on the twin boundaries. The selected areas SA1, SA2, and SA3 are located on the boundaries of the matrix-primary twins, primary-secondary twins, and secondary-ternary twins, respectively. When these hierarchical twins are all tilted to the $[0\bar{1}1]$ zone axis, the BCC matrix is oriented near [135]. This approximated $[0\bar{1}1]$–[135] zone-axis relationship between the primary band and matrix also corresponds to {332}<113> twinning [44–46]. In addition to {332}<113> type high-order twinning, as shown in Fig. 5(d–f), {112}<111> nanotwins can also be activated in primary {332}<113> twin. In Fig. 5(d), the $(112)[11\bar{1}]$ twins and parallel dislocations are triggered on the (112) and $(\bar{1}\bar{1}2)$ plane of a primary {332}<113> twins band, respectively. The formation of these high-density dislocations and high-order twins inside the primary twin further strengthens the primary twin itself and contributes to the work-hardening effect associated with {332}<113> mechanical twinning [22].

Probably due to the complexity of the local stress concentration, as shown in Fig. 6, the hierarchical mechanical twinning process is much more complex from area to area even inside a single primary {332}<113> twinning band. The matrix is near the [531] axis corresponding to the $[1\bar{1}0]$ axis of primary {332}<113> twins. There are secondary {332}<113> twins, {112}<111> twins variant 1, and

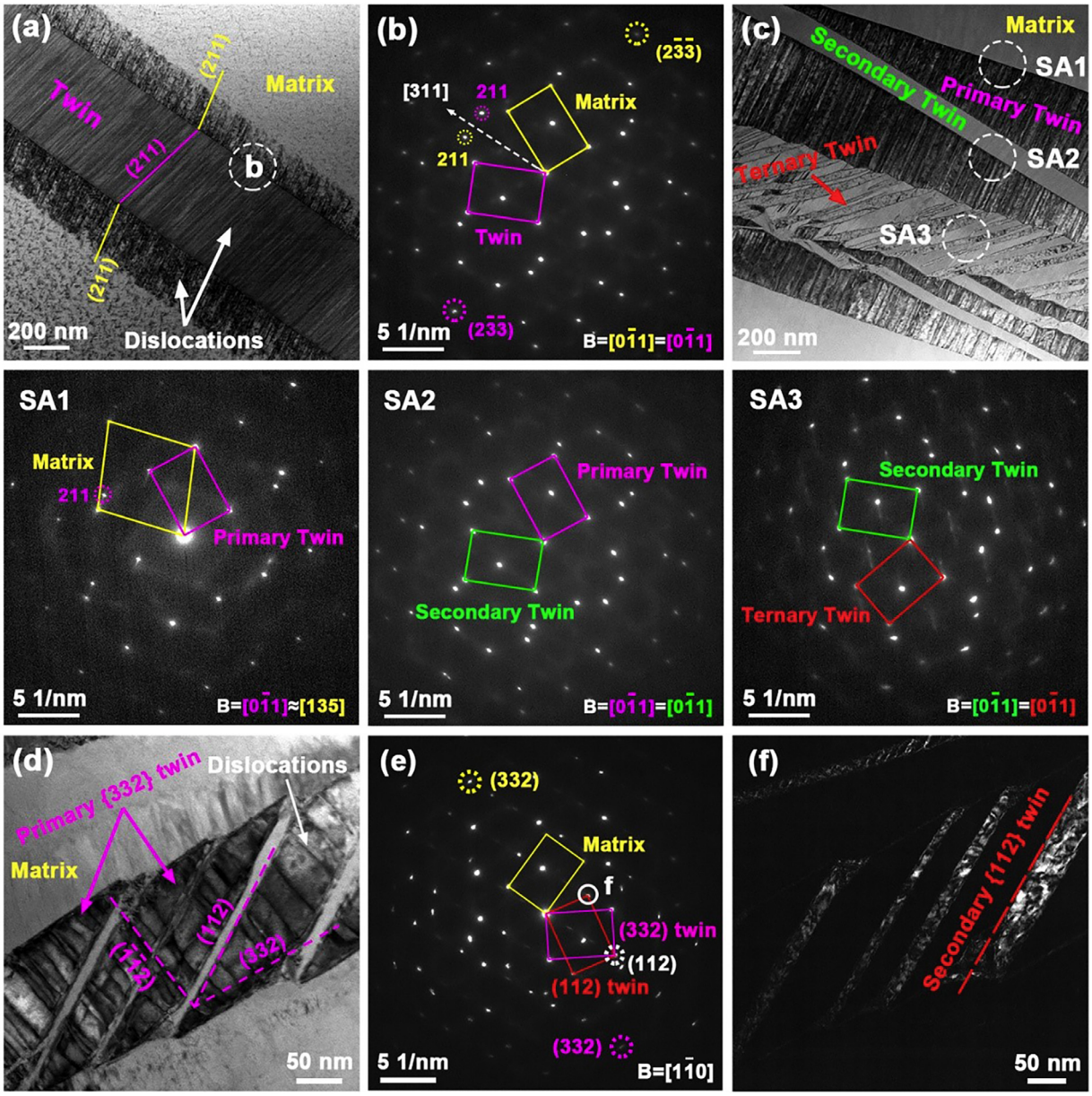

Fig. 5. Nanoscale hierarchical twinning structure in the deformed $TiZrHfNb_{0.5}$ alloy at 77K: (a, b) BF image of the {332}<113> twin and corresponding SAED pattern after a 10 % tensile strain; (c) primary, secondary, and ternary {332}<113> twins with corresponding SAEDs of zones of SA1, SA2 and SA3 after a 10 % tensile strain; (d–f) BF image, SAED and DF image of secondary {112}<111> secondary twins after a 20 % tensile strain.

{112}<111> twins variant 2 in selected areas SA1, SA2, and SA3, respectively. In SA4, also shown in Fig. 6(d), ternary {112}<111> twins activated in relatively coarse secondary {332}<113> twins within the primary {332}<113> twin band. Generally, the width of activated {332}<113> twins has a range from micrometer to nanometer. The high-order {332}<113> and {112}<111> twins are more prone to be activated inside {332}<113> twin bands. However, the width of {112}<111> twins is only limited to the nanometer scale. As shown in Fig. 6, the {112}<111> twins can only be activated as the high-order twins in the hierarchical twinning structure meanwhile without other twins inside. The high-stress concentration in primary or secondary {332}<113> twin bands would contribute to the activation of high-order {112}<111> nano twins.

Besides the high-order twinning process inside primary {332}<113> twin bands, the intersection of different {332}<113> twin variants plays an important role in the formation of the hierarchical twinning substructure. In Fig. 7(a), with increasing the tensile strain from 10 to 35 % (the largest uniform tensile strain), the BCC matrix is fragmented into sub-micron areas, which are difficult to characterize by EBSD. Fig. 7(b–e) shows the process of the twinning intersection-induced matrix refinement under the same zone axis of $[011]_{Matrix}$-near $[135]_{Twin}$. In Fig. 7(b, c), after a 10 % tensile strain, {332}<113> twin bands including variants 1 and 2 with a thickness of 100 nm or less are activated in the BCC matrix. In Fig. 7(c), a high density of dislocations is formed in association with the {332}<113> twins. In addition, the intersection of these twins also triggers internal high-order twinning. With tensile strain increasing to 35 %, the complex high-order twinning substructure combined with high-density dislocations makes it difficult to distinguish twins and the BCC matrix. The BCC matrix segmented by highly deformed twinning channels becomes regularly arranged nano-scale islands. Fig. 7(f) shows the intersection of two {332}<113> twin variants that share a common rotation

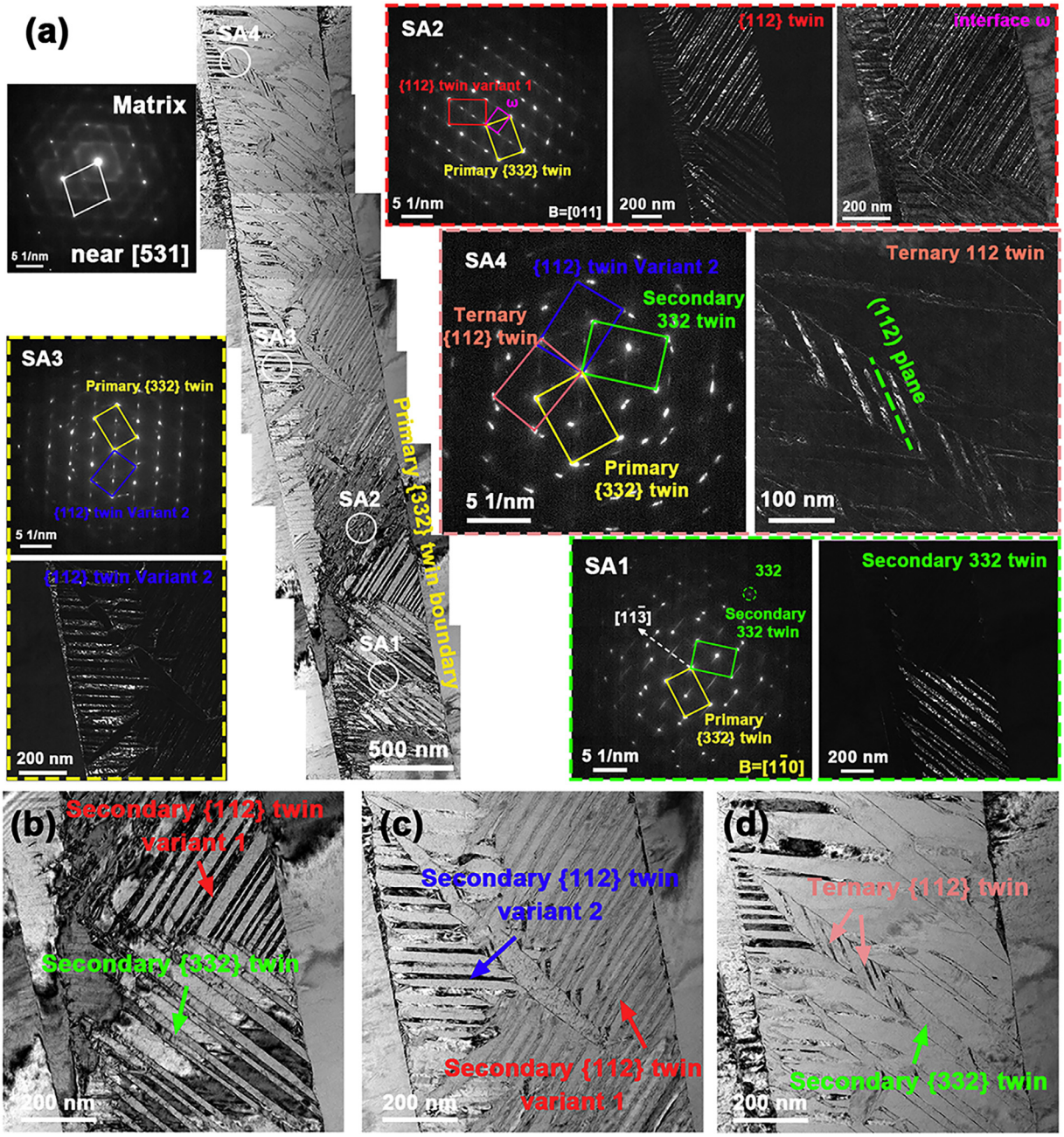

Fig. 6. The complexity of hierarchical twins in the 10 % tensile deformed $TiZrHfNb_{0.5}$ alloy at 77K: (a) BF of primary {332}<113> twin and SAEDs of the areas SA1, SA2, SA3, and SA4 with corresponding DF images attached; (b–d) zoom-in images of secondary {332}<113> twins, secondary {112}<111> variant 1, secondary {112}<111> variant 2, and ternary {112}<111> twins.

axis [101] of the BCC matrix during twinning with the BCC matrix decorated with high-density dislocations. These twins' intersection together with high-order twinning contributes to the progressive refinement of the initial BCC matrix.

3.3. Strength-ductility adjustment by increasing the Nb content

To further adjust the strength-ductility of the $TiZrHfNb_{0.5}$ alloy, the niobium content is appropriately increased. As shown in Fig. 8(a), the mechanical properties of $TiZrHfNb_x$ alloys are significantly affected by slightly increasing the Nb content at 77 K. The yield strength increased from 865 MPa of the $TiZrHfNb_{0.5}$ ($Nb_{0.5}$) alloy to 890 MPa of the $TiZrHfNb_{0.55}$ ($Nb_{0.55}$) alloy and 1075 MPa of $TiZrHfNb_{0.6}$ ($Nb_{0.6}$) alloy. A 20 % uniform elongation is still obtained for $Nb_{0.55}$ and $Nb_{0.6}$ alloys, though the increase of Nb inevitably decreases the tensile elongation of $TiZrHfNb_x$ alloys at 77 K. In comparison, the RT tensile properties have little change in both tensile strength and elongation, which can be interpreted by the same dislocation slip-dominated mechanisms (Fig. S2). At RT, although these alloys exhibit excellent plasticity (no cracking after 80 % cold rolling and over 20 % total elongation), the intrinsic poor strain-hardening ability makes them immediately enter the diffuse necking process soon after yielding. During the uniaxial tensile test, sufficient strain-hardening ability is a necessary prerequisite for high ductility, i.e., large uniform elongation [10,29,47]. The true stress-strain curves and strain-hardening rates, Θ, of $Nb_{0.5}$, $Nb_{0.55}$, and $Nb_{0.6}$ alloys at 77 K are plotted in Fig. 8(b). At the beginning of plastic deformation, corresponding to the elastic-plastic

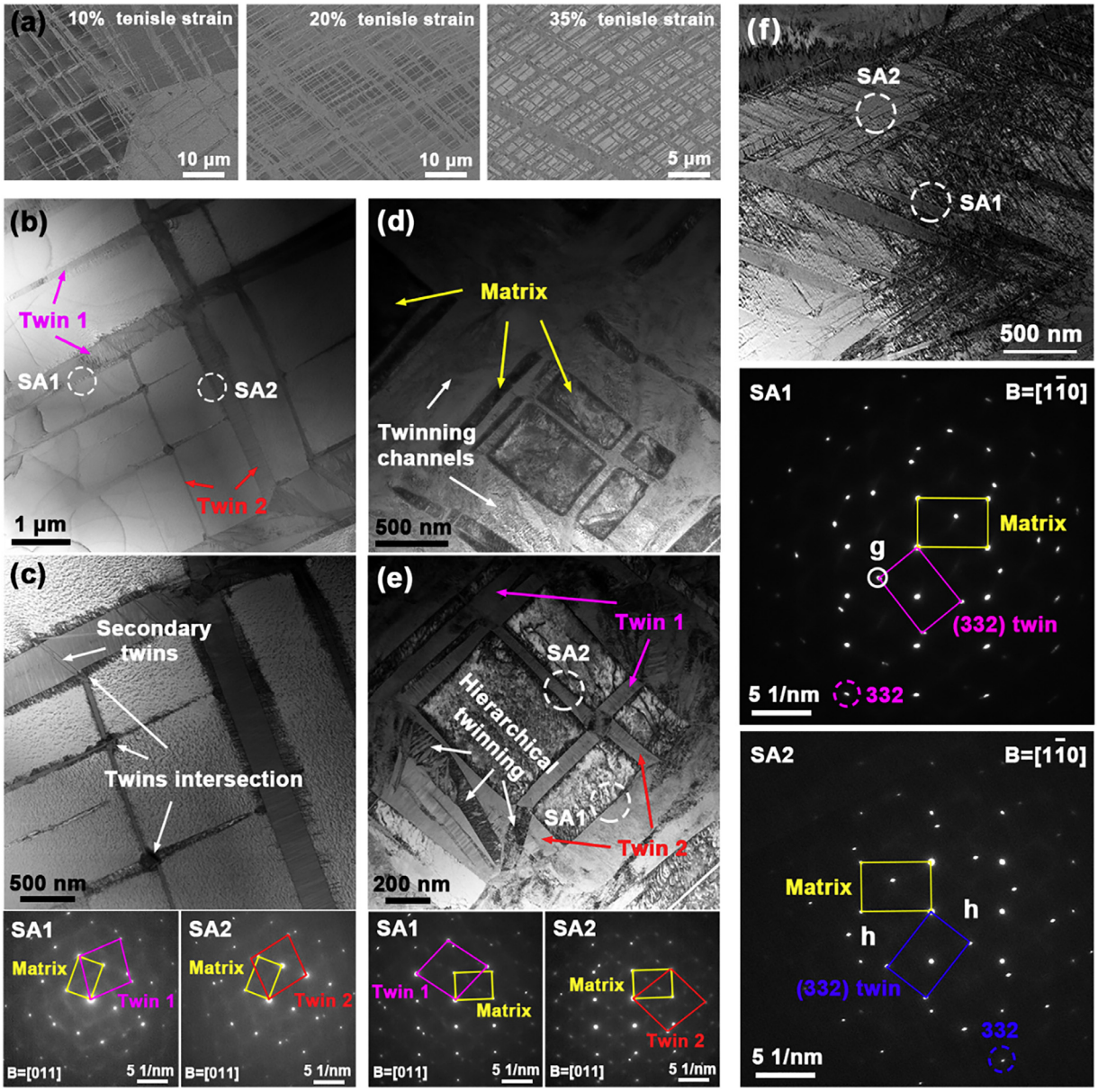

Fig. 7. Twins intersection in the deformed $TiZrHfNb_{0.5}$ alloy at 77 K: (a) deformation substructure evolution after 10 %, 20 %, and 35 % tensile strains; (b–e) intersected {332}<113> twins after 10 % and 35 % tensile strains along the $[531]_{twin}$ axis, respectively; (f) intersected {332}<113> twins after a 20 % tensile strain along the $[1\bar{1}0]_{twin}$ axis.

transition, the strain-hardening rate, Θ, drops sharply for all alloys. Then, the Θ decreases monotonously until the initiation of necking in the $Nb_{0.6}$ alloy, while they recover obviously from a 5 to 15 % true strain for $Nb_{0.5}$ and $Nb_{0.55}$ alloys. According to the Considère criterion [48], the necking points, i.e. the intersections of the true stress-strain curves and corresponding strain-hardening rate curves were marked out in Fig. 8(b). As compared in Fig. 8(c), in the ultimate tensile strength versus uniform elongation map, the $TiZrHfNb_x$ in this study and TiZrHfNbTa alloy deformed at 77 K stand out from all the previously reported refractory HEAs deformed at room temperature. Compared with the TiZrHfNbTa alloy [7], the uniform elongation is improved in $TiZrHfNb_x$ alloys although the strength is sacrificed. It is worth mentioning that the recently reported $TiZrHfNb_xTa_{0.2}$ alloys (x = 0.3, 0.4) [49] also exhibit great strength-ductility combination at 77 K owing to the hybrid mechanisms, including the planar dislocation slip, strain-induced phase transition, and twinning.

For $TiZrHfNb_x$ alloys, the increase of the Nb content suppresses the activation of {332}<113> twinning. As shown in Figs. 1 and 2, twinning occurs inside almost all grains of the $Nb_{0.5}$ alloy at 77 K after 10 % and 20 % strains. While twinning is only activated in partial grains of the $Nb_{0.5}$ and $Nb_{0.6}$ alloy with low multiplication during deformation, as presented in Fig. 9(a, b). As an example, Fig. 9(c) presents an enlarged view of a grain divided by intersected {332}<113> twins confirmed by stereographic projections pole figures (Fig. 9(e1–e5)). The further detailed hierarchical {332}<113> deformation twins were identified in Figs. S3 and S4.

At 77 K, according to Fig. 9, the deformation process of partial grains of the $TiZrHfNb_{0.6}$ alloy is dominated by the intersected {332}<113> mechanical twins, while the rest of grains are solely dominated by the dislocation glide. To further confirm this result, Figs. 10 and 11 present the nanoscale deformation substructures within the {332}<113> mechanical twinning-dominated and dislocation slip-dominated grains, respectively. In Fig. 10, after 10 % ten-

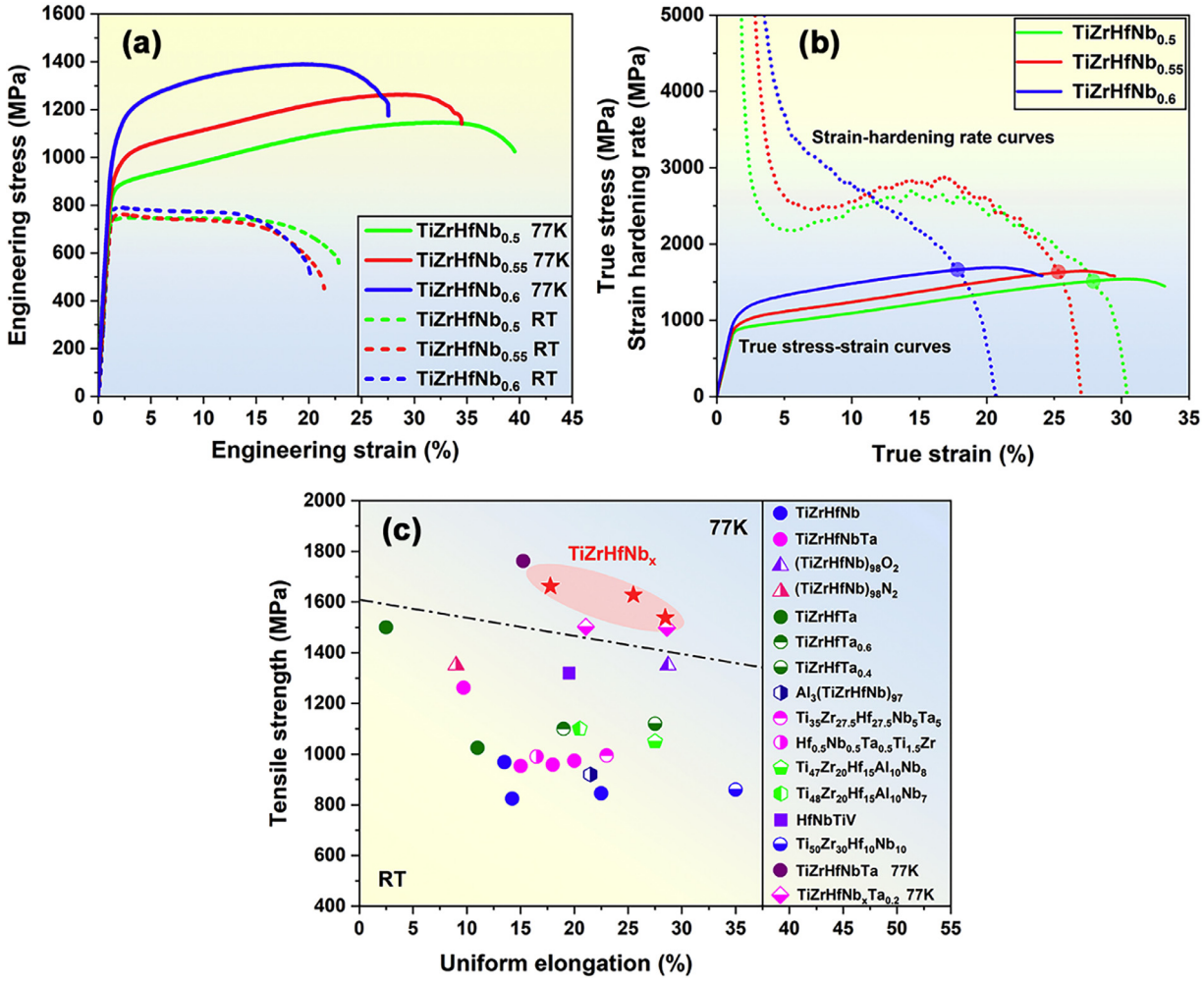

Fig. 8. Tensile properties of $TiZrHfNb_x$ (x = 0.5, 0.55, and 0.6) alloys at RT and 77 K: (a) tensile engineering stress-strain curves; (b) the intersections of true stress-strain curves and corresponding strain-hardening rate curves indicates the necking points; (c) tensile strength versus uniform elongation of the $TiZrHfNb_x$ alloys at 77 K, compared with the existing refractory HEAs in the Refs. [4,30,31,49–57].

sile strain at 77 K, two {332}<113> twin variants intersected with each other to divide the original BCC matrix. At the same time, high-density dislocations are activated inside the matrix and twin bands to accommodate the overall plastic deformation. In Fig. 11, multiplanar screw dislocation slip and dislocation bands can be observed along with the formation of dislocation pinning loops and dipoles.

For comparison, as exhibited in Fig. 12, tensile tests of the equiatomic TiZrHfNb alloy are also performed at 77 K. In Fig. 12(a), the equiatomic TiZrHfNb alloy presents sound tensile plasticity at 77 K given nearly the 20 % total elongation and ductile dimples on the fracture surface. However, the deformation relying solely on dislocation glide (Fig. 12(b, c)) results in a poor strain-hardening ability, which generates negligible ductility after yielding.

4. Discussion

For metallic materials, plasticity is important for forming metals into the desired shape, which is mostly controlled by the available slip systems with mobile dislocations [47,58]. However, good plasticity does not guarantee high ductility which needs enough strain-hardening to evade strain localization by activating effective barriers, including short-range order [4,59], nano-precipitates [60,61], dislocations substructures [62,63], twins [12–14,64], phase boundaries [30,65,66], heterogeneous grains structures [67,68], etc., to block gliding dislocations and force them to accumulate.

At RT, $TiZrHfNb_x$ alloys in this study exhibit excellent plasticity (can be rolled to an 80 % thickness reduction without cracking and exhibit significant necking until ductile fracture during tension) despite the strain-hardening ability being negligible. For $TiZrHfNb_x$ and other series metastable HEAs/MEAs within Ti-Zr-Hf-Nb-Ta compositional space, the formation of {332}<113> mechanical twinning in BCC phase is extremely rare at room temperature. This would be caused by the inherently large lattice distortion and short-range order [69], which inhibits the lattice shear and shuffle process for twinning [70]. For TiZrHfNb alloy, the favored Ti-Zr pairs' chemical short-range order has been theoretically predicted [71,72].

According to the results above, it can be summarized that decreasing the deformation temperature can effectively improve the strain-hardening ability of $TiZrHfNb_x$ alloys to ensure appreciable ductility by activating hierarchically mechanical twinning. With decreasing the temperature, if the flow stress rises more rapidly than the twinning stress, a transition from the dislocation slip to mechanical twinning can be envisaged [38,73]. Different from FCC alloys (e.g., austenite steels [12,19,74] and 3d transition HEAs [14,36,37,75]), which rely on strong strain hardening to reach critical twinning stress after significant dislocation accumulation, the strong temperature-dependent yield stress originated from non-

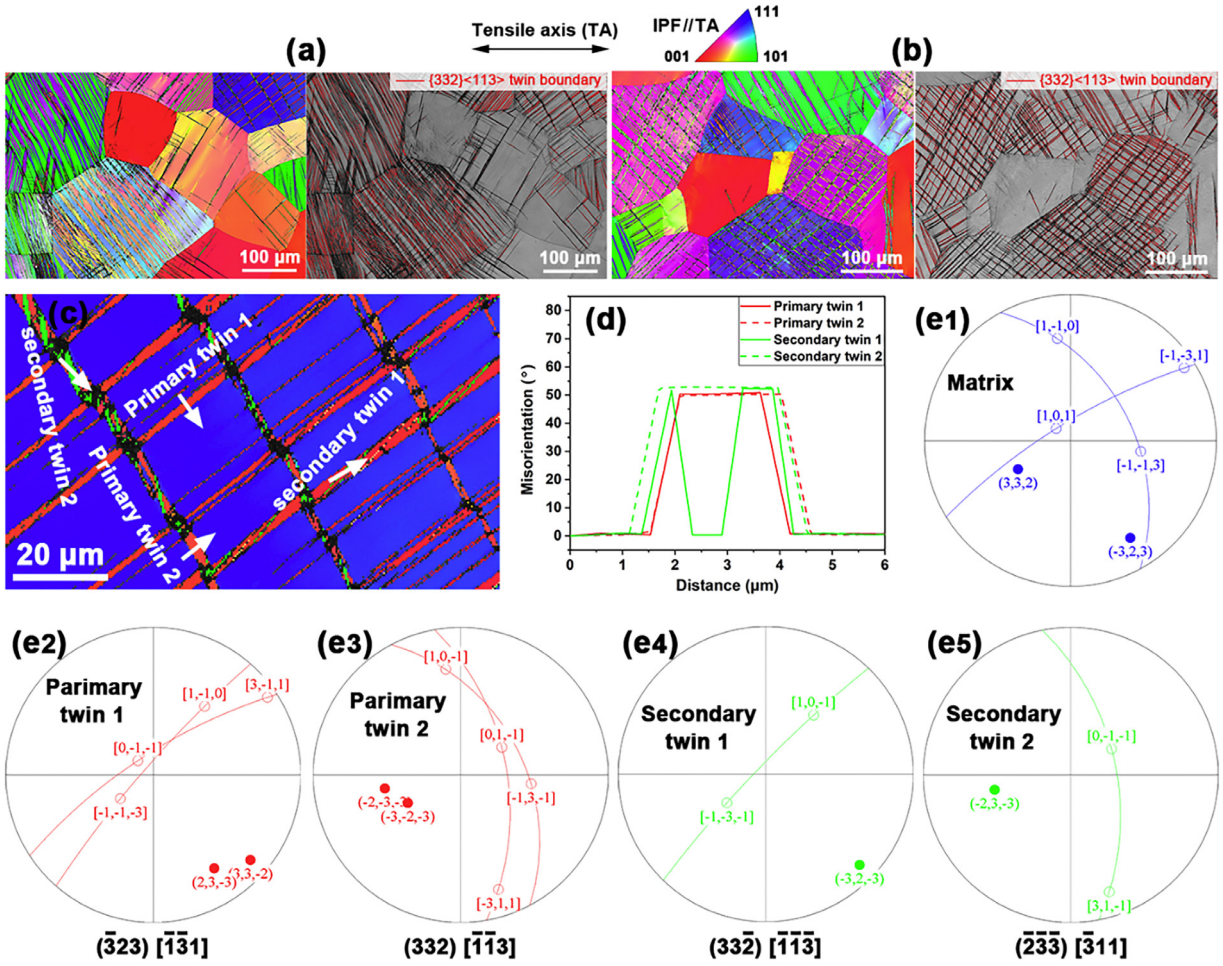

Fig. 9. Microstructure of $TiZrHfNb_{0.55}$ and $TiZrHfNb_{0.6}$ alloys after 10 % tensile strain at 77K: (a, b) IPFs and band contrast maps with {332}<113> twin boundaries of $TiZrHfNb_{0.55}$ and $TiZrHfNb_{0.6}$ alloys, respectively; (c) enlarged view of grain in (a); (d) misorientation profiles along the lines in (c); (e1–e5) stereographic projection of the BCC matrix and primary twins variants and secondary twins variants.

planar screw dislocation core [58] of BCC alloys make the twinning usually activated before macro-yielding with decreasing temperature [38,73]. For BCC $TiZrHfNb_x$ alloys in this investigation, the poor strain-hardening ability leads to premature necking with negligible ductility during RT tensile deformation. Therefore, the activation of twinning is critical to ensure a sufficient strain-hardening ability soon after yielding. In Fig. 1(e), the {332}<113> twinning bands are distributed in almost all the grains after a 5 % tensile strain. Even in the 10 % strained $TiZrHfNb_{0.5}$ alloy at 77 K, as shown in Figs. 5(a, c) and 7(b, c), basically no dislocations exist in the BCC matrix subdivided by {332}<113> twinning bands. When temperature decreased to 127 K, as shown in Fig. S5, intersected {332}<113> twins and {112}<111> nano twins have been triggered for $TiZrHfNb_{0.5}$ alloys, which confirmed once again the important role of hierarchical twinning substructures.

Fig. 13(a–c) give the size distribution of the initial grains, {332}<113> and {112}<111> mechanical twins. The initial structure exhibits a single BCC phase with an average grain size of 92 μm. The width of the activated {332}<113> twins spans from several microns to ten nanometers with an average of 1.7 μm and 182 nm distinguished by EBSD and TEM, respectively. In contrast, the {112}<111> nano twins with an average width of 10.6 nm and only existed within the pre-activated {332}<113> twins. The schematical illustration of the TWIP effect in $TiZrHfNb_x$ alloys at cryogenic temperatures is shown in Fig. 13(d). After yielding, the {332}<113> mechanical twins from the micro to nanometer scale are activated in coarse recrystallized BCC grains. As the plastic deformation proceeds, the number of twins increases and the widespread twin intersections contribute to forming a three-dimensional twin network. At the same time, the multi-scale high-order twins (secondary and/or ternary twins), including {332}<113> and {112}<111> twins formed within the activated twin bands. These two simultaneous structural evolution processes contribute to the formation of a hierarchical twinning architecture in the $TiZrHfNb_x$ alloy at 77 K. The hierarchical-twinning substructure formation progressively segments the initially coarse grains into the nanoscale, as shown in Fig. 6, which contributes to the high strain-hardening ability and in turn the uniform elongation of $TiZrHfNb_x$ alloys at 77 K. In this study, the twinning-induced plasticity generally has two strain-hardening origins [12,13,76], i.e., the dynamic Hall-Petch effect-induced isotropic hardening and back stress-induced kinematic hardening. At 77 K, the continuously formed {332}<113> twins dynamically reduce the mean free path of dislocations by progressively segmenting the initial BCC matrix, thereby improving the dislocation storage and ensuring the flow stress. In addition, the dislocation pile-up in front of twin obstacles would generate a long-range back stress which is continuously concentrated with increasing the twinning interface. In this investigation, the coactivation and intersection of primary, secondary, and even ternary {332}<113> twin variants construct a three-dimensional architecture, thereby effectively impeding the propagation of dislocations. In addition to strengthening, the de-

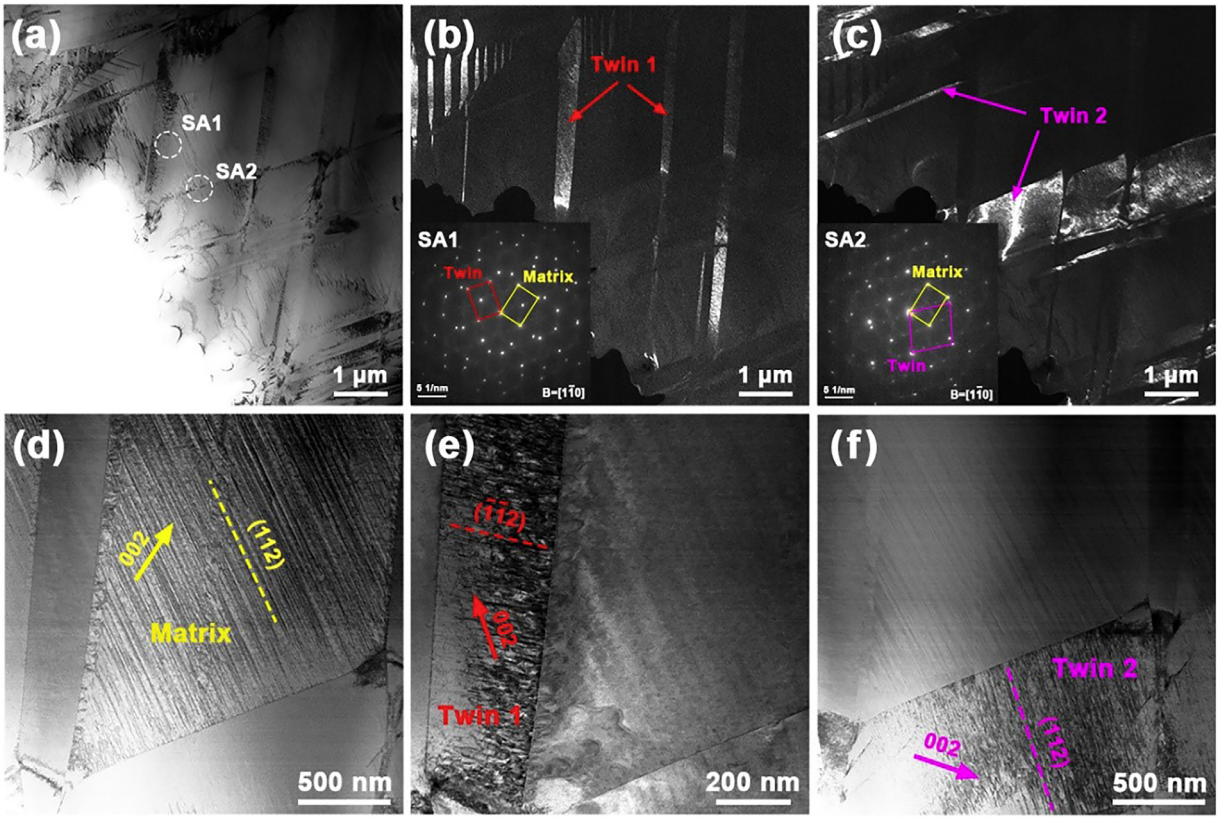

Fig. 10. {332}<113> twins intersection inside one grain of $TiZrHfNb_{0.6}$ alloy with 10 % interrupted tensile strain at 77 K: (a) BF image; (b, c) DF images and corresponding SAEDs; (d–f) dislocations in the divided matrix and twinning bands.

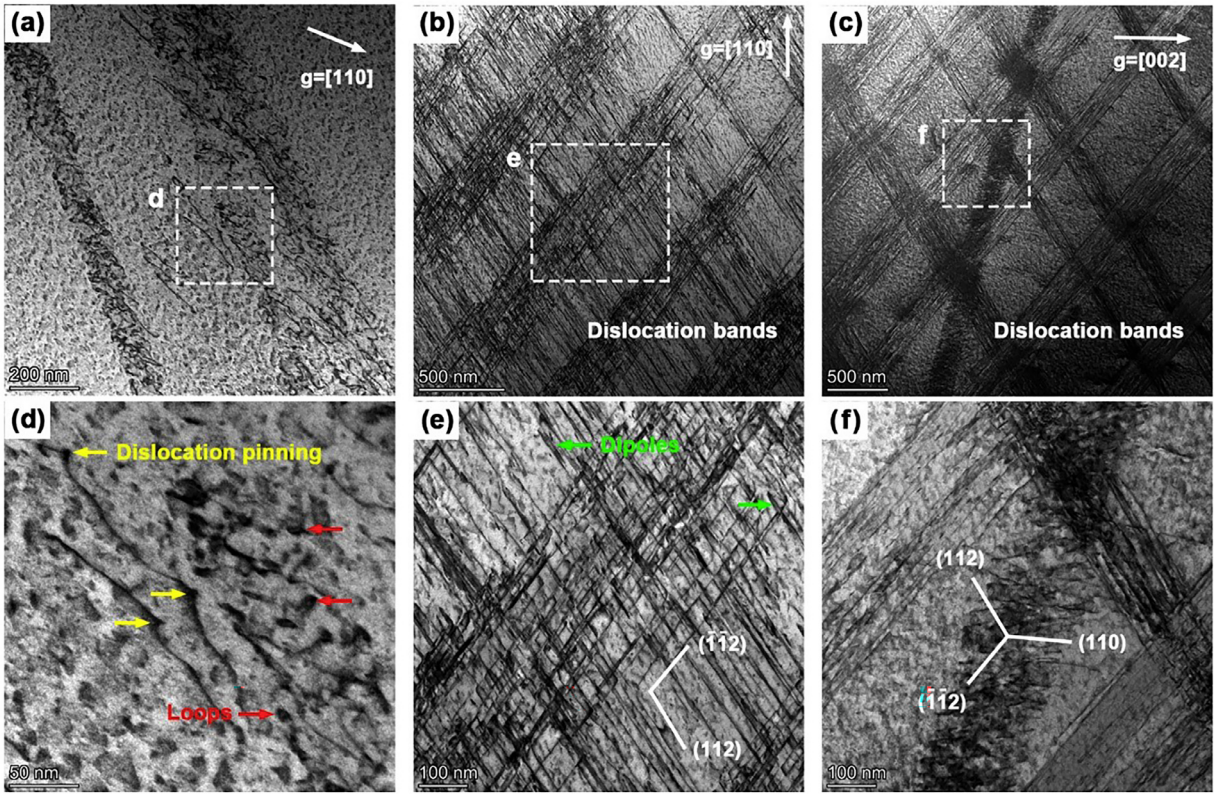

Fig. 11. Dislocations glide inside grains of the $TiZrHfNb_{0.6}$ alloy with 10 % interrupted tensile strain at 77 K: (a, d) dislocations pinning and loops; (b, e) dislocations intersection on {112} planes; (c, f) deformation bands with high-density dislocations.

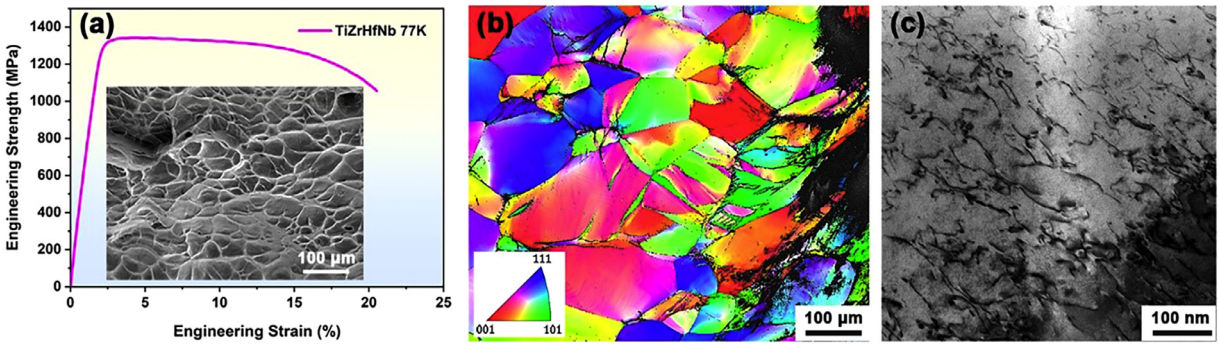

Fig. 12. Tensile properties and deformation substructure of equiatomic TiZrHfNb alloy at 77 K: (a) engineering tensile curve and fracture morphology; (b) IPF of deformed grains near tensile fracture surface and (c) TEM-BF image of dislocations.

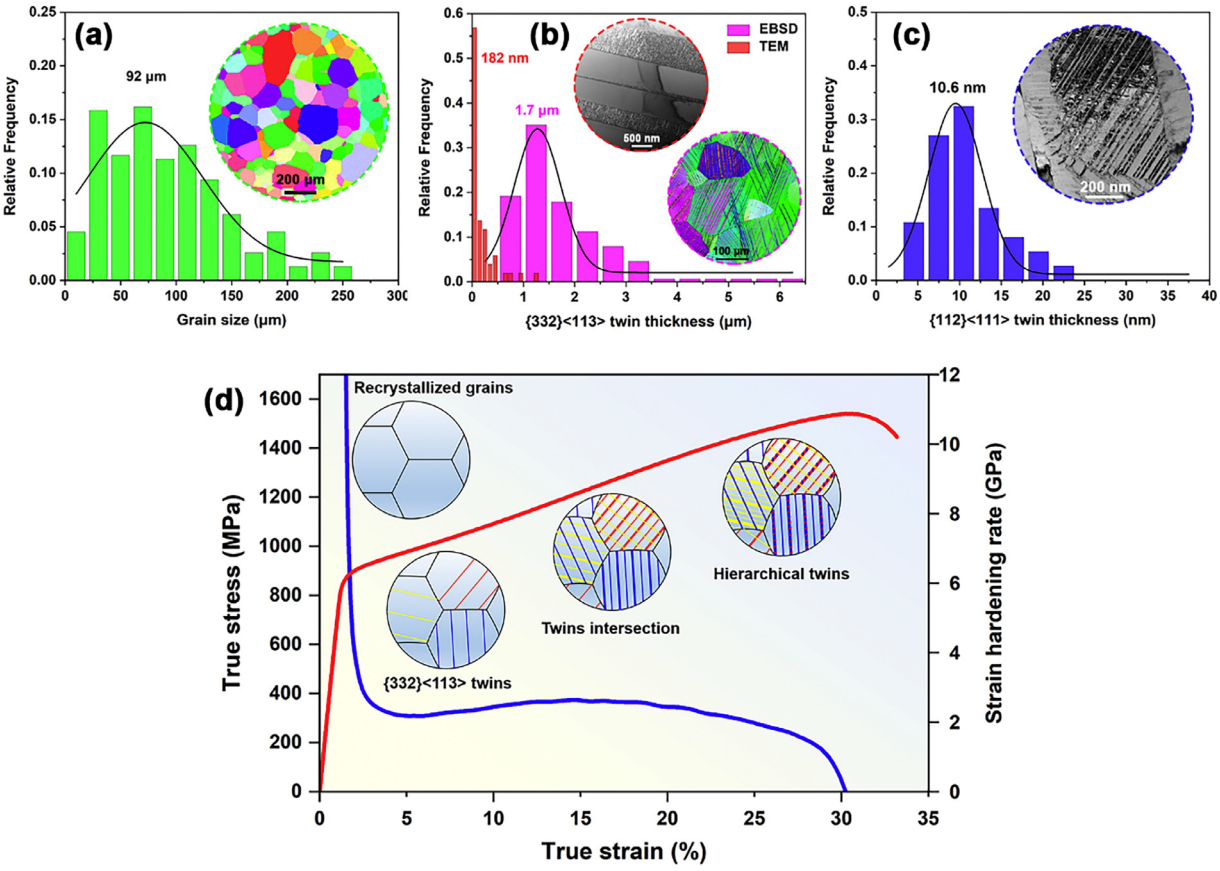

Fig. 13. Quantitative statistics of (a) initial grain size; (b) {332}<113> twins thickness and (c) {112}<111> twins thickness; (d) schematic illustration of the TWIP effect in $TiZrHfNb_x$ alloys.

velopment of hierarchical twinning substructures also provides the dislocation-slip channels and {112}<111> nano-twinning nucleation sites to improve ductility and postpone premature cracking under high-stress concentrations [16,77].

The activation of hierarchical twinning above can be attributed to two aspects. As an unusual twinning process, the occurrence of {332}<113> twinning is closely related to the $\beta \rightarrow \alpha$" phase transformation. It has been confirmed that the transformed α" phase can assist the formation of {332}<113> mechanical twins in metastable β-Ti alloys through $\alpha" \rightarrow \beta$ reverse phase transition [22,34]. This α" transformation-assisted activation process tends to induce inherent defects like dislocations (Figs. 5(a, d) and 6(b)) which might cause self-activated hierarchical secondary twins inside [78]. In addition, the frequent intersection of {332}<113> twinning bands (Figs. 4(a) and 7(c)) or dislocations pile up around the twins would induce the local stress concentration and therefore trigger the secondary even ternary twinning events [44]. This "stress concentration" explanation is consistent in that the {112}<111> twin stress is higher than that of {332}<113> twins.

In addition to temperature, the Nb content is another critical factor governing the competition between the mechanical twinning and dislocation glide of $TiZrHfNb_x$ alloys. And more specifically, decreasing the temperature and Nb-content tailoring are two prerequisites to activating hierarchical {332}<113> twinning in the $TiZrHfNb_x$ system. In the TiZrHf-Nb pseudo-binary compositional space, consistent with the binary Ti-Nb, the isomorphous element, Nb, can stabilize the BCC structure when added into TiZrHf which consists of polymorphic elements. For $TiZrHfNb_x$ alloys, {332}<113> twinning activated within the compositional space from $Nb_{0.5}$ to $Nb_{0.6}$ with an appropriate BCC phase stabil-

ity. For a much more stable TiZrHfNb alloy, the deformation is fully controlled by dislocation glide at 77 K (exhibits high yield strength and weak strain hardening ability). For BCC alloys, the yield strength rises steeply with decreasing temperature by dislocation slip, while the twinning stress is less changed [38]. This rule also applies to the $TiZrHfNb_x$ alloys in this work, with increasing the Nb content (from $Nb_{0.5}$ to $Nb_{0.6}$ alloys), qualitatively, the dislocations glide plays an increasingly important role during deformation at 77 K which contributes to the increased yield strength of $TiZrHfNb_x$ alloys. At 77 K, the {332}<113> twinning dominated deformation in the $Nb_{0.5}$ alloy brings excellent strain-hardening and the highest elongation while the increasing role of dislocation slip with increasing Nb content significantly improves the yield strength and inevitably reduces the strain-hardening and elongation in $Nb_{0.6}$ alloy.

5. Conclusions

In summary, this investigation demonstrates that {332}<113> hierarchical mechanical twinning dominated TWIP effect can be engineered in $TiZrHfNb_x$ HEAs to dramatically improve the strain-hardening ability and strength-ductility combination. The exploration of these TWIP-RHEAs would provide notable insights into the deformation mechanisms of refractory multicomponent systems and contribute to designing high-performance refractory HEAs. The main conclusions can be drawn below:

(1) Within the Ti-Zr-Hf-Nb multicomponent compositional space, a large number of deformation twins can be activated during deformation by decreasing both the stability of the BCC phase and deformation temperature, which contributes to twinning-induced plasticity by dramatical improving the strain-hardening ability.
(2) For $TiZrHfNb_{0.5}$ alloys, hierarchical complex twinning networks gradually formed through continuous nucleation, growth, activation of high-order twin bands, and frequent twins intersection process during deformation at 77 K. The width of activated {332}<113> twins has a wide range from several microns to ten nanometers with an average of 1.7 μm, which contributes to the generation of multiscale twining frameworks and dominates the dynamic Hall-Petch effect. The high-order {332}<113> and {112}<111> twins are activated inside primary {332}<113> twin bands. In contrast, {112}<111> nano twins with an average width of 10.6 nm only existed within the pre-activated {332}<113> twins and without other twins inside.
(3) It has been verified in this investigation that the strength-ductility of $TiZrHfNb_x$ alloys can further be flexibly adjusted by slightly increasing the Nb content at 77 K. With the increase of the Nb content from $Nb_{0.5}$ to $Nb_{0.6}$, the dominant role of {332}<113> deformation twins gradually decreases meanwhile enhancing the yield strength for $TiZrHfNb_{0.6}$ alloy.

Declaration of competing interest

The authors declare that they have no known competing financial interests or personal relationships that could have appeared to influence the work reported in this paper.

Acknowledgments

This work was supported by the National Natural Science Foundation of China (Nos. 52301163 and 51821001) and the National Key R&D Program of China (No. 2022YFB3706800). P.K. Liaw very much appreciates the support from (1) the National Science Foundation (Nos. DMR-1611180, 1809640, and 2226508) and (2) the US Army Research Office (Nos. W911NF-13–1–0438 and W911NF-19–2–0049).

Supplementary materials

Supplementary material associated with this article can be found, in the online version, at doi:10.1016/j.jmst.2023.11.047.

References

[1] O.N. Senkov, G.B. Wilks, D.B. Miracle, C.P. Chuang, P.K. Liaw, Intermetallics 18 (2010) 1758–1765.
[2] D.B. Miracle, M.H. Tsai, O.N. Senkov, V. Soni, R. Banerjee, Scr. Mater. 187 (2020) 445–452.
[3] O. El-Atwani, N. Li, M. Li, A. Devaraj, J.K.S. Baldwin, M.M. Schneider, D. Sobieraj, J.S. Wrobel, D. Nguyen-Manh, S.A. Maloy, E. Martinez, Sci. Adv. 5 (2019) eaav2002.
[4] Z. Lei, X. Liu, Y. Wu, H. Wang, S. Jiang, S. Wang, X. Hui, Y. Wu, B. Gault, P. Kontis, D. Raabe, L. Gu, Q. Zhang, H. Chen, H. Wang, J. Liu, K. An, Q. Zeng, T.G. Nieh, Z. Lu, Nature 563 (2018) 546–550.
[5] O.N. Senkov, J.M. Scott, S.V. Senkova, D.B. Miracle, C.F. Woodward, J. Alloys Compd. 509 (2011) 6043–6048.
[6] L. Lilensten, J.P. Couzinié, L. Perrière, A. Hocini, C. Keller, G. Dirras, I. Guillot, Acta Mater. 142 (2018) 131–141.
[7] S. Wang, M. Wu, D. Shu, G. Zhu, D. Wang, B. Sun, Acta Mater. 201 (2020) 517–527.
[8] G. Dirras, L. Lilensten, P. Djemia, M. Laurent-Brocq, D. Tingaud, J.P. Couzinié, L. Perrière, T. Chauveau, I. Guillot, Mater. Sci. Eng. A 654 (2016) 30–38.
[9] E.P. George, W.A. Curtin, C.C. Tasan, Acta Mater. 188 (2020) 435–474.
[10] E. Ma, X. Wu, Nat. Commun. 10 (2019) 5623.
[11] Y. Wei, Y. Li, L. Zhu, Y. Liu, X. Lei, G. Wang, Y. Wu, Z. Mi, J. Liu, H. Wang, H. Gao, Nat. Commun. 5 (2014) 3580.
[12] B.C. De Cooman, Y. Estrin, S.K. Kim, Acta Mater. 142 (2018) 283–362.
[13] G.H. Zhao, X. Xu, D. Dye, P.E.J. Rivera-Díaz-del-Castillo, Acta Mater. 183 (2020) 155–164.
[14] Y. Deng, C.C. Tasan, K.G. Pradeep, H. Springer, A. Kostka, D. Raabe, Acta Mater. 94 (2015) 124–133.
[15] B. Gludovatz, A. Hohenwarter, D. Catoor, E.H. Chang, E.P. George, R.O. Ritchie, Science 345 (2014) 1153–1158.
[16] Z. Zhang, H. Sheng, Z. Wang, B. Gludovatz, Z. Zhang, E.P. George, Q. Yu, S.X. Mao, R.O. Ritchie, Nat. Commun. 8 (2017) 14390.
[17] D.R. Steinmetz, T. Jäpel, B. Wietbrock, P. Eisenlohr, I. Gutierrez-Urrutia, A. Saeed-Akbari, T. Hickel, F. Roters, D. Raabe, Acta Mater. 61 (2013) 494–510.
[18] J. Gao, Y. Huang, D. Guan, A.J. Knowles, L. Ma, D. Dye, W.M. Rainforth, Acta Mater. 152 (2018) 301–314.
[19] I. Gutierrez-Urrutia, D. Raabe, Acta Mater. 59 (2011) 6449–6462.
[20] H. Idrissi, K. Renard, D. Schryvers, P.J. Jacques, Scr. Mater. 63 (2010) 961–964.
[21] S. Sadeghpour, S.M. Abbasi, M. Morakabati, A. Kisko, L.P. Karjalainen, D.A. Porter, Scr. Mater. 145 (2018) 104–108.
[22] M.J. Lai, C.C. Tasan, D. Raabe, Acta Mater. 111 (2016) 173–186.
[23] X. Min, X. Chen, S. Emura, K. Tsuchiya, Scr. Mater. 69 (2013) 393–396.
[24] D. Wei, X. Li, J. Jiang, W. Heng, Y. Koizumi, W.M. Choi, B.J. Lee, H.S. Kim, H. Kato, A. Chiba, Scr. Mater. 165 (2019) 39–43.
[25] J. Su, D. Raabe, Z. Li, Acta Mater. 163 (2019) 40–54.
[26] S. Huang, H. Huang, W. Li, D. Kim, S. Lu, X. Li, E. Holmstrom, S.K. Kwon, L. Vitos, Nat. Commun. 9 (2018) 2381.
[27] Q. Lin, J. Liu, X. An, H. Wang, Y. Zhang, X. Liao, Mater. Res. Lett. 6 (2018) 236–243.
[28] J. Liu, X. Guo, Q. Lin, Z. He, X. An, L. Li, P.K. Liaw, X. Liao, L. Yu, J. Lin, L. Xie, J. Ren, Y. Zhang, Sci. China Mater. 62 (2018) 853–863.
[29] O.N. Senkov, D.B. Miracle, K.J. Chaput, J.P. Couzinie, J. Mater. Res. 33 (2018) 3092–3128.
[30] L. Lilensten, J.P. Couzinié, J. Bourgon, L. Perrière, G. Dirras, F. Prima, I. Guillot, Mater. Res. Lett. 5 (2017) 110–116.
[31] H. Huang, Y. Wu, J. He, H. Wang, X. Liu, K. An, W. Wu, Z. Lu, Adv. Mater. 29 (2017) 1701678.
[32] L. Wang, C. Fu, Y. Wu, Q. Wang, X. Hui, Y. Wang, Mater. Sci. Eng. A 748 (2019) 441–452.
[33] L. Zhang, H. Fu, S. Ge, Z. Zhu, H. Li, H. Zhang, A. Wang, H. Zhang, Mater. Charact. 142 (2018) 443–448.
[34] P. Castany, Y. Yang, E. Bertrand, T. Gloriant, Phys. Rev. Lett. 117 (2016) 245501.
[35] B. Gludovatz, A. Hohenwarter, K.V. Thurston, H. Bei, Z. Wu, E.P. George, R.O. Ritchie, Nat. Commun. 7 (2016) 10602.
[36] F. Otto, A. Dlouhy, C. Somsen, H. Bei, G. Eggeler, E.P. George, Acta Mater. 61 (2013) 5743–5755.
[37] G. Laplanche, A. Kostka, C. Reinhart, J. Hunfeld, G. Eggeler, E.P. George, Acta Mater. 128 (2017) 292–303.
[38] J.W. Christian, S. Mahajan, Prog. Mater. Sci. 39 (1995) 1–157.
[39] M. Yang, L. Zhou, C. Wang, P. Jiang, F. Yuan, E. Ma, X. Wu, Scr. Mater. 172 (2019) 66–71.
[40] S. Wang, M. Wu, D. Shu, B. Sun, Mater. Lett. 264 (2020) 127369.
[41] X.H. Min, K. Tsuzaki, S. Emura, T. Sawaguchi, S. Ii, K. Tsuchiya, Mater. Sci. Eng. A 579 (2013) 164–169.
[42] T. Kawabata, S. Kawasaki, O. Izumi, Acta Mater. 46 (1998) 2705–2715.
[43] T. Furuhara, K. Kishimoto, T. Maki, Mater. Trans. JIM 35 (1994) 843–850.
[44] J. Zhang, Y. Fu, Y. Wu, B. Qian, Z. Chen, A. Inoue, Y. Wu, Y. Yang, F. Sun, J. Li, F. Prima, Mater. Res. Lett. 8 (2020) 247–253.
[45] Y. Yang, P. Castany, Y.L. Hao, T. Gloriant, Acta Mater. 194 (2020) 27–39.

[46] W. Wang, X. Zhang, J. Sun, Mater. Charact. 142 (2018) 398–405.
[47] Y.T. Zhu, X.L. Wu, Mater. Today Nano 2 (2018) 15–20.
[48] C.L. Yang, Z.J. Zhang, P. Zhang, Z.F. Zhang, Acta Mater. 136 (2017) 1–10.
[49] X. Wen, L. Zhu, M. Naeem, H. Huang, S. Jiang, H. Wang, X. Liu, X. Zhang, X.L. Wang, Y. Wu, Z. Lu, Scr. Mater. 231 (2023) 115434.
[50] S. Wang, D. Wu, H. She, M. Wu, D. Shu, A. Dong, H. Lai, B. Sun, Mater. Sci. Eng. C 113 (2020) 110959.
[51] Y. Wu, Y. Cai, T. Wang, J. Si, J. Zhu, Y. Wang, X. Hui, Mater. Lett. 130 (2014) 277–280.
[52] C.C. Juan, M.H. Tsai, C.W. Tsai, W.L. Hsu, C.M. Lin, S.K. Chen, S.J. Lin, J.W. Yeh, Mater. Lett. 184 (2016) 200–203.
[53] O.N. Senkov, S.L. Semiatin, J. Alloys Compd. 649 (2015) 1110–1123.
[54] Y. Wu, J. Si, D. Lin, T. Wang, W.Y. Wang, Y. Wang, Z. Liu, X. Hui, Mater. Sci. Eng. A 724 (2018) 249–259.
[55] S. Sheikh, S. Shafeie, Q. Hu, J. Ahlström, C. Persson, J. Veselý, J. Zýka, U. Klement, S. Guo, J. Appl. Phys. 120 (2016) 164902.
[56] Z. An, S. Mao, T. Yang, C.T. Liu, B. Zhang, E. Ma, H. Zhou, Z. Zhang, L. Wang, X. Han, Mater. Horiz. 8 (2021) 948–955.
[57] S. Wang, S. Lu, M. Wu, D. Wang, G. Zhu, C. Yang, D. Shu, B. Sun, L. Vitos, Mater. Sci. Eng. A 832 (2022) 142476.
[58] D. Hull, D.J. Bacon, Introduction to Dislocations, Elsevier Ltd. 4th ed., 2001.
[59] R. Zhang, S. Zhao, J. Ding, Y. Chong, T. Jia, C. Ophus, M. Asta, R.O. Ritchie, A.M. Minor, Nature 581 (2020) 283–287.
[60] T. Yang, Y. Zhao, Y. Tong, Z. Jiao, J. Wei, J. Cai, X. Han, D. Chen, A. Hu, J. Kai, Science 362 (2018) 933–937.
[61] S. Jiang, H. Wang, Y. Wu, X. Liu, H. Chen, M. Yao, B. Gault, D. Ponge, D. Raabe, A. Hirata, Nature 544 (2017) 460–464.
[62] B. He, B. Hu, H. Yen, G. Cheng, Z. Wang, H. Luo, M. Huang, Science 357 (2017) 1029–1032.
[63] C. Yang, Z. Zhang, T. Cai, P. Zhang, Z. Zhang, Sci. Rep. 5 (2015) 1–7.
[64] S. Zhao, R. Zhang, Q. Yu, J. Ell, R.O. Ritchie, A.M. Minor, Science 373 (2021) 1363–1368.
[65] M. Marteleur, F. Sun, T. Gloriant, P. Vermaut, P.J. Jacques, F. Prima, Scr. Mater. 66 (2012) 749–752.
[66] S.H. Kim, H. Kim, N.J. Kim, Nature 518 (2015) 77–79.
[67] K. Lu, Science 345 (2014) 1455–1456.
[68] X. Wu, M. Yang, F. Yuan, G. Wu, Y. Wei, X. Huang, Y. Zhu, Proc. Natl. Acad. Sci 112 (2015) 14501–14505.
[69] F. Walsh, A. Abu-Odeh, M. Asta, MRS Bull. 48 (2023) 753–761.
[70] R. Niu, X. An, L. Li, Z. Zhang, Y.W. Mai, X. Liao, Acta Mater. 223 (2022) 117460.
[71] A. Chen, Y. Pan, J. Dai, W. Fu, X. Song, Mater. Today Commun. 36 (2023) 106922.
[72] K. Xun, B. Zhang, Q. Wang, Z. Zhang, J. Ding, E. Ma, J. Mater. Sci. Technol. 135 (2023) 221–230.
[73] M. Meyers, O. Vöhringer, V. Lubarda, Acta Mater. 49 (2001) 4025–4039.
[74] S. Curtze, V.T. Kuokkala, Acta Mater. 58 (2010) 5129–5141.
[75] G. Laplanche, A. Kostka, O.M. Horst, G. Eggeler, E.P. George, Acta Mater. 118 (2016) 152–163.
[76] O. Bouaziz, J. Moon, H.S. Kim, Y. Estrin, Scr. Mater. 191 (2021) 107–110.
[77] X.H. An, Science 373 (2021) 857–858.
[78] Q. Zhu, Q.S. Huang, Y.Z. Tian, S.C. Zhao, Y.B. Chen, G. Cao, K.X. Song, Y.J. Zhou, W. Yang, Z. Zhang, X.H. An, H.F. Zhou, J.W. Wang, Sci. Adv. 8 (2022) eabn8299.